

The application of multivariate statistical methods to NMR imaging

C.A. Glasbey
Biomathematics and Statistics Scotland

and S.M. Glidewell
Scottish Crop Research Institute

August 24, 2000

Corresponding author:

Dr C.A. Glasbey
Biomathematics and Statistics Scotland
JCMB, King's Buildings
Edinburgh EH9 3JZ
Scotland

Tel: (44) +131 650 4899
Fax: (44) +131 650 4901
email: c.glasbey@bioss.sari.ac.uk

Abstract

Statistical methods are used to integrate the information content in multivariate NMR images which had been obtained using different instrumental settings. Empirical and mechanistic models of multivariate pixel values are compared, making use of a novel reparametrisation of the mechanistic parameters to improve numerical stability. A new approach is presented to integrating the information using colour image displays. Projection pursuit is used to identify optimal instrumental settings in synthetic images. Methods are illustrated using seven cross-sectional NMR microscopy images of a blackberry which was chosen as typical of fruit specimens with hard tissue distributed in a soft matrix.

Key words: Blackberry, Entropy, Fruit, Principal components, Projection pursuit, Pseudo-colour images, *Rubus fruticosus*, Synthetic MRI.

1 Introduction

Nuclear Magnetic Resonance (NMR) imaging, referred to in the medical literature as MRI, is a powerful technique for the non-invasive visualisation of the internal structure of objects. This is of particular advantage in medicine, in which field the early development of MRI was fostered, but has many applications in, for example, process engineering where the ability to distinguish between different chemical species and to yield information simultaneously on the structure, concentration distribution and flow processes occurring within a manufacturing plant is particularly useful (Gladden and Alexander, 1996). In plant science, little or no sample preparation is required and changes over time in specimen anatomy can be observed. NMR imaging also has a primary advantage over other imaging modalities in that dynamic as well as density parameters can be spatially resolved and information inferred about the biophysical state of cellular water. This results from the sensitivity of the NMR signal, via the spin-lattice (T_1) and spin-spin (T_2) relaxation times, to molecular motion on a broad range of time scales from the sub-microsecond to the quasi-static.

In the context of plant imaging, contrast is used to define difference in grey-scale between two forms of tissue and the discernibility of a structure of given size is determined by a combination of contrast and signal-to-noise ratio. Clearly, any of the factors which affect signal-to-noise ratio may also influence contrast and these can be classified into those which arise from the tissue itself (intrinsic factors) and those from the experimental variables (extrinsic factors). Intrinsic factors include spatial variations in T_1 , T_2 , T_{2*} , $T_{1\rho}$, spin density, chemical shift, the presence of paramagnetics, and the net flow and diffusion of tissue water. Extrinsic factors include the chosen image sequence, the spectrometer magnetic field B_0 , the magnetic field gradients applied, the pulse sequence repetition time (T_R), and the time to echo (T_E).

Considerable effort has been devoted to image analysis of medical/clinical NMR images in attempts to derive diagnostic tests for, for example, the presence of malignancies, atherosclerosis (Merickel et al., 1991, 1993) or osteoporosis (Majumdar et al., 1989). Increasing use of Functional Magnetic Resonance Imaging (fMRI) has led to the development of time series methods to pinpoint, for example, active areas of the brain corresponding to stimuli or function (Bull-

more et al., 1996; Rogowska et al., 1995; Backfrieder et al., 1996; Lange and Zeger, 1997). Plants intrinsically have higher-contrast NMR images than animals, due in large measure to the presence of intercellular gas spaces which give rise to magnetic susceptibility discontinuities which cause local loss of signal as a consequence of rapid T_2 relaxation. Image processing of plant NMR images has been applied in the detection of bruising in apples (Zion et al., 1995).

Determination of optimum imaging parameters and the generation of synthetic images have been investigated for clinical applications using a variety of methods including the derivation of a generalised expression for tissue discrimination between pairs of tissue types (Fox and Henson, 1986), a method which requires knowledge of the fractional differences in the intrinsic parameters for each tissue type. Dreher and Börnert (1988) established an algorithm to maximise contrast criteria and derive optimal pulse sequence parameters and Pedersen et al. (1995) have used multivariate analysis incorporating PCA to investigate PET images. Multivariate image analysis has been applied to brain NMR images (Windig et al., 1998; Antalek et al., 1998) and PCA has been used to analyse sets of correlated NMR images (Geladi et al., 1992a,b; Grahn et al., 1989; Grahn and Saaf, 1992). In the main, the aim of these papers has been to generate optimum extrinsic factors (pulse sequence parameters) for a given set of intrinsic parameters.

Integration of information from several images into a single image, for a particular specimen at a particular time, allows comparison of images of different specimens or investigation of temporal variations. For example, Fig 1 shows seven cross-sectional images of a blackberry, obtained using a soft 90° –hard 180° spin echo pulse sequence on a Bruker AMX300 microimaging system with different instrumental settings. The blackberry fruit was chosen as it has hard seeds distributed in a soft watery matrix, and thus gave a wide range of contrast in images acquired with different instrumental parameters. The seven images can be considered as a multidimensional image, in that there are seven signals or variates measured at each location in the image. The purpose of this paper is to explore multivariate statistical methods for integrating the information content of these seven images. In §2 we compare and contrast empirical and mechanistic models for these data. Then, in §3 we consider ways of displaying this information. Finally, in §4 we discuss the results.

2 Models

Linear models can be constructed for multivariate NMR images (Zhu et al., 1994; Soltanian-Zadeh et al., 1996). These are empirical in that they take no account of information about how the signals were obtained. However, they form a baseline against which to judge mechanistic models which are derived from the physics of NMR (Majumdar et al., 1989; Lange et al., 1991; Sinha et al., 1992). We first consider empirical models in §2.1, then mechanistic ones in §2.2.

2.1 Empirical models

Let Y_{ij} denote the i th pixel value in image j , where there are n pixels in each of m images. In the case of Fig 1, $n = 256 \times 256 = 65536$ and $m = 7$. Because we do not make any use in

this paper of the spatial distribution of pixels, to keep the notation as simple as possible we will only use a single subscript to denote a pixel rather than the conventional double subscript. There can be a lot of redundancy in the information contained in multiple NMR images, so there are benefits in reducing their number to p , say, where $p < m$. The best p -dimensional representation of Y , that is the one which minimises the mean square error

$$\frac{1}{nm} \sum_{i=1}^n \sum_{j=1}^m (Y_{ij} - f_{ij})^2, \quad (1)$$

is given by

$$f_{ij} = \mu_j + \sum_{k=1}^p \alpha_{jk} Z_{ik} \quad \text{for } i = 1, \dots, n; j = 1, \dots, m, \quad (2)$$

(Krzanowski, 1988). Here, Z is an $n \times p$ matrix with Z_{ik} being the i th element in the k th principal component of Y , μ is an m -vector with μ_j being the mean pixel value in image j , and the coefficients in the $m \times p$ matrix, α , are obtained by regressing Y on Z . The principal components, Z , are linear combinations of the images:

$$Z_{ik} = \sum_{j=1}^m (Y_{ij} - \mu_j) \beta_{jk} \quad \text{for } i = 1, \dots, n; k = 1, \dots, p,$$

where β is a $m \times p$ matrix with β_{jk} being the j th element in the k th eigenvector of the variance-covariance matrix of Y , V , where

$$V_{jk} = \frac{1}{n-1} \sum_{i=1}^n (Y_{ij} - \mu_j)(Y_{ik} - \mu_k) \quad \text{for } j = 1, \dots, m; k = 1, \dots, m.$$

The number of parameters used in this empirical model, given by eq.(2), is m for μ , together with np for α and $(mp - p(p+1)/2)$ for β (the term $p(p+1)/2$ arises because the β s are unit vectors which are constrained to be orthogonal). Table 1 gives μ , V and β for a 3-dimensional model (i.e. $p = 3$). This accounts for 99.5% of the variation in Y , using $(3n + 22)$ parameters, and the mean square error, eq. (1), is 5.76. It can be seen from V that the images, particularly the second to the sixth, are highly correlated, and that variances increase with means. The first principal component is a weighted average of the seven images, with weights approximately in proportion to the means of the images. The second principal component is a contrast between the seventh image and the rest, and is therefore an effect due to T_E . The third principal component is a contrast between the sixth image and the first five, and is therefore an effect due to T_R .

An alternative empirical model is obtained if we omit μ from the specification of f , giving

$$f'_{ij} = \sum_{k=1}^p \alpha'_{jk} Z'_{ik} \quad \text{for } i = 1, \dots, n; j = 1, \dots, m,$$

where

$$Z'_{ik} = \sum_{j=1}^m Y_{ij} \beta'_{jk} \quad \text{for } i = 1, \dots, n; k = 1, \dots, p.$$

This constrains the regression to pass through the origin and makes the model more directly comparable with the mechanistic model in §2.2. Term β'_{jk} is the j th element in the k th eigenvector of the non-centred variance-covariance matrix of Y , V' , where

$$V'_{jk} = \frac{1}{n-1} \sum_{i=1}^n Y_{ij} Y_{ik} \quad \text{for } j = 1, \dots, m; k = 1, \dots, m.$$

The β' , also given in Table 1, are very similar to the β : the mean square error is slightly increased to 6.10, but the model requires seven fewer parameters.

2.2 Mechanistic models

A mechanistic model for spin-echo images is given by Glad and Sebastiani (1995)

$$f_{ij} = \rho_i e^{-T_{Ej}/T_{2i}} \left(1 - e^{-T_{Rj}/T_{1i}}\right) \quad \text{for } i = 1, \dots, n; j = 1, \dots, m. \quad (3)$$

This is a nonlinear function of the instrumental settings T_E and T_R in image j , denoted T_{Ej} and T_{Rj} , and non-negative parameters ρ , T_1 and T_2 in pixel i , denoted ρ_i , T_{1i} and T_{2i} . Parameters can be estimated by minimising

$$\sum_{j=1}^m (Y_{ij} - f_{ij})^2 \quad (4)$$

with respect to ρ_i , T_{1i} and T_{2i} , separately for each pixel, i , subject to the non-negativity constraint on the parameters, using a nonlinear optimisation algorithm. We encountered instabilities in estimating the parameter values for some pixels. So, we reparametrised the model in terms of three fitted values, in order to gain stability (Ross, 1990, pp. 24-27). Let γ_1 denote the fitted value for particular instrumental settings T_E and T_R , let γ_2 be the fit for T_E and $2T_R$, and let γ_3 be the fit for $T'_E (> T_E)$ and $2T_R$. Therefore, from eq. (3),

$$\gamma_1 = \rho e^{-T_E/T_2} \left(1 - e^{-T_R/T_1}\right), \quad (5)$$

$$\gamma_2 = \rho e^{-T_E/T_2} \left(1 - e^{-2T_R/T_1}\right), \quad (6)$$

$$\gamma_3 = \rho e^{-T'_E/T_2} \left(1 - e^{-2T_R/T_1}\right), \quad (7)$$

where, to simplify the notation, from now we omit the pixel i subscript. We can obtain ρ , T_1 and T_2 from γ_1 , γ_2 and γ_3 , as follows. By dividing eq. (6) by eq. (5),

$$\frac{\gamma_2}{\gamma_1} = \frac{1 - e^{-2T_R/T_1}}{1 - e^{-T_R/T_1}} = 1 + e^{-T_R/T_1},$$

which can be re-expressed as

$$T_1 = \frac{-T_R}{\log(\gamma_2/\gamma_1 - 1)}. \quad (8)$$

Also, by dividing eq. (6) by eq. (7),

$$\frac{\gamma_2}{\gamma_3} = \frac{e^{-T_E/T_2}}{e^{-T'_E/T_2}},$$

which can be re-expressed as

$$T_2 = \frac{T'_E - T_E}{\log(\gamma_2/\gamma_3)}. \quad (9)$$

Finally, substituting eq. (8) and eq. (9) in eq. (5), we obtain

$$\rho = \frac{\gamma_1}{e^{-T_E/T_2}(1 - e^{-T_R/T_1})}.$$

For ρ , T_1 and T_2 to all be non-negative, necessary and sufficient constraints on γ are:

$$\gamma_1 \geq 0, \quad 2\gamma_1 \geq \gamma_2 \geq \gamma_1, \quad \gamma_2 \geq \gamma_3 \geq 0.$$

This parameterisation, with $T_E = 10$, $T_R = 250$ and $T'_E = 50$, was fitted to the $n = 256^2$ pixels in the $m = 7$ images in Fig 1. A sequential quadratic programming algorithm (Numerical Algorithms Group, 1993, routine E04UPF) was used to iteratively minimise the sum of squares, eq. (4). Fig 2 illustrates the fit for a single pixel, in the centre of the upper right globe in Fig 1. The fitted values for all pixels are displayed in image form in Fig 3. Note that, we could fit this model to as few as three images. Also, if the three images had instrumental settings of (T_E, T_R) , $(T_E, 2T_R)$ and $(T'_E, 2T_R)$, then parameters could be estimated directly, circumventing the need for iterative optimisation.

The mean square error is 6.82 for this mechanistic model, which requires $3n$ parameters. Therefore, the fit is slightly poorer than for the empirical linear models in §2.1, for which mean square errors of 5.76 and 6.10 were obtained. Therefore, it is apparent that the model assumptions in eq. (3) are not entirely appropriate. A more general mechanistic model for spin-echo images is given by Sebastiani and Barone (1991)

$$f_{ij} = \rho_i \exp\left[-\frac{T_{Ej}}{T_{2i}}\right] \left\{ 1 + \exp\left[-\frac{T_{Rj}}{T_{1i}}\right] - 2 \exp\left[-\frac{T_{Rj} - T_{Ej}/2}{T_{1i}}\right] \right\}.$$

However, this is still an approximation, as it is a common feature of biological systems that T_2 relaxation is multi-exponential (Callaghan, 1991). This model was fitted to the data, but the fit was only marginally better than before, with a mean square error is 6.48. Therefore we continue to use the simpler functional form given by eq. (3) in the rest of the paper.

It would appear from Fig 3 that noise levels are reasonably low. However, when we display in Fig 4 the original set of parameters, ρ , T_1 and T_2 , we see that they are not well estimated, and estimates of ρ , T_1 are very highly correlated. The noise levels are higher than in Fig 3 because we are extrapolating beyond the range of the data. It is possible to use neighbouring pixels to smooth the results, either after model fitting, or as an integral part of model fitting (Garnier et al., 1993; Glad and Sebastiani, 1995). However, we consider it to be sounder statistical practice to avoid extrapolation, which we do in §3.

3 Image displays

3.1 Colour image

According to the mechanistic model, eq. (3), all the information in Fig 1 is encapsulated in Fig 3. The empirical model also supports the notion that the data signal is three dimensional, at most. This is convenient, because a tri-variate signal lends itself to colour display, because the human colour vision system is also three dimensional: our eyes respond to a combination of red, green and blue signals. However, care must be taken in representing information in colour. If, for example, the three images in Fig 3 were simply assigned to red, green and blue in a single image, then the result will appear almost wholly as shades of grey because the three signals are so highly correlated. One way round this problem of correlation is to assign the colours to the principal component transformation of the images (Glasbey and Horgan, 1995, ch. 2). This could be done either by performing a principal components analysis on Fig 3, or taking the results from the empirical model in §2.1. In either case, the resulting image would be colourful, but not necessarily easy to interpret. Someone experienced at studying grey-level NMR images would have difficulty knowing what the different colours represented. This could be overcome in time, by users familiarising themselves with a particular form of display, provided that a standard transformation could be established, so that colours were used in a consistent way.

We propose an alternate method, which is both colourful and easier to interpret. We take one image (in our case, we choose to use γ_2 , the expected NMR image at instrumental settings $T_E, 2T_R$) as a grey-level image, and superimpose on it, in colour, the additional information in the other two images, γ_1 and γ_3 (the expected NMR image at instrumental settings of T_E, T_R and $T'_E, 2T_R$, respectively). Fig 5 shows scatterplots of the pixel values in γ_2 plotted against those γ_1 and γ_3 . In both cases they can be seen to be highly correlated, especially the relationship between γ_2 and γ_1 . The additional information in γ_1 over and above that given by γ_2 , can be obtained by subtracting the regression of γ_1 on γ_2 . This is given by

$$\gamma'_1 = \gamma_1 - \phi\gamma_2, \quad \text{where } \phi = \frac{\sum_i(\gamma_{1i} - \bar{\gamma}_1)(\gamma_{2i} - \bar{\gamma}_2)}{\sum_i(\gamma_{2i} - \bar{\gamma}_2)^2}$$

and $\bar{\gamma}$ denotes the mean pixel value in an image. Fig 6 shows the resulting image, obtained by subtracting 74% of γ_2 from γ_1 , and then rescaling. In fact, this is very similar to the image of the third principal component in Table 1, which we have not displayed. Fig 6 also shows the resulting image after subtracting 43% of γ_2 from γ_3 . This turns out to be very similar to an image of the second principal component.

If we now assign these two images to red and green, and γ_2 to grey, Fig 7 is produced. This is achieved by assigning to red (R), green (G) and blue (B) the following signals:

$$\begin{aligned} R &= \gamma_2 \{1 - (1 - \gamma''_1)\gamma''_3\}, \\ G &= \gamma_2 \{1 - \gamma''_1(1 - \gamma''_3)\}, \\ \text{and } B &= \gamma_2 \{1 - (1 - \gamma''_1)(1 - \gamma''_3)\}, \end{aligned}$$

where γ''_1 denotes a rescaled version of γ'_1 , which takes values between 0 and 1, and similarly for γ''_3 . (Rather than using the smallest and largest values in γ'_1 as our limits, to enhance the

colour in Fig 7 we used the mean values of γ'_1 and γ'_3 plus and minus two standard deviations as the limits for rescaling to γ''_1 and γ''_3 .) We claim that Fig 7 contains all the information in the original seven images, and is easy to interpret. The image intensity shows the signal at $T_R = 500$, $T_E = 10$, red areas show where the signals for smaller values of T_R are proportionally stronger, green areas show where the signals for larger values of T_E are proportionally stronger, yellow areas show where both conditions apply and grey areas show where neither condition applies. Expressed another way, red shows tissues where T_1 is small, green shows where T_2 is large, yellow shows both and grey shows neither.

3.2 Synthetic images

We can use the mechanistic model, eq. (3), to generate synthetic images for any other settings of the instrumental variables. Alternatively, we could combine together the information in Fig 3 in ways that do not correspond to any physically-realizable image. For example, by obtaining the first principal component we would have that linear combinations of images which maximises the variance in pixel values. In NMR imaging, interest usually centres on finding images that maximise contrast between different tissues, and this may or may not correspond to the variance being maximised. Other measures have been proposed in the statistical literature which are more likely to maximise contrast, and the method is called ‘projection pursuit’ (Jones and Sibson, 1987). There are many criteria (Cook et al., 1993), one of the simplest being to minimise the entropy

$$-\sum_c p_c \log p_c$$

where p_c denotes the proportion of pixel values in cell c of a histogram which has been standardised to have zero mean and unit variance, and the sum is over all histogram cells.

We searched for values of T_E and T_R which minimised the entropy of a synthetic image. We restricted attention to $200 \geq T_E \geq 10$ and $1000 \geq T_R \geq 50$, both because this ensures that the synthetic images are physically realisable and because otherwise we would have to extrapolate from the fitted values and results become very susceptible to the effects of noise. To avoid outliers having undue influence, pixel values were constrained to be within three standard deviations of the mean, and the histogram cell width used was 0.1 standard deviations. We found that several local minima existed, each of which is of potential importance in highlighting particular tissue contrasts. Fig 8 shows the three smallest minima, again with pixel values constrained to be within three standard deviations of the mean.

4 Discussion

The statistical approach we have described here has two main benefits: it results in data compression as the information from seven images has all been displayed in the three images in Fig 3 and in a single image in Fig 7, and it allows for objective selection of the instrumental parameters T_E and T_R which produce the best images, by projection pursuit. In this case ‘best’ has been taken to mean having the greatest contrast in intensity values. Plant tissues are

characterised by long T_1 values and short T_2 s and this, together with the presence of intercellular gas spaces leads to the possibility of greater contrast than in animal tissues. Automatic selection of instrumental parameters is possibly of greater importance in NMR imaging of plant tissues, where many different species with widely differing characteristics are investigated, than in medical MRI, where a single species (*Homo sapiens*) is studied: even superficially similar plant species and organs such as strawberry and raspberry fruits can require very different T_E and T_R settings to produce good images (Goodman et al., 1992, 1996). There is thus great potential advantage in being able to record three images relatively quickly and then calculate the optimum values of T_E and T_R to maximise image contrast.

By restricting ourselves to interpolation rather than extrapolation, good signal to noise ratios have been obtained in the synthetic images, indicating that further image acquisition would be unnecessary. The good fit between calculated and actual images for identical values of T_E and T_R shown in Fig 2 corroborates this. By using larger blocks of pixels for the calculations, it would be possible to obtain better signal/noise ratios (at the expense of spatial resolution) for extrapolated values of T_E and T_R , in particular long T_R values, thus allowing a preview of a long T_R image without expending large amounts of instrument time or risking sample deterioration for possibly little return in terms of image quality.

It could be argued that projection pursuit is in essence no different from what an experienced operator would expect to produce in normal practice, with the operator's knowledge and experience replaced by the calculation step. It can, nonetheless, save machine time and give an objective result on each occasion. It is interesting to note that the values of the parameters T_E and T_R in the three smallest minima in Fig 8 are perhaps not the values which would have been selected by such an operator; in particular the lack of a T_1 -weighted image with short T_E and T_R is unusual. The presence of relatively bright blackberry seeds in Fig 8(a), with a short T_E of 17ms, suggests that the T_2 for the seeds was not too short to have given a T_1 -weighted image. The values of T_E and T_R in Fig 8(a) are tending towards a spin density image, and the relative contrasts in different parts of the image resemble those of ρ in Fig 4, but with greatly improved signal to noise. Many spin density images of plant tissue show little contrast and it is probably only the presence of the hard seeds in this specimen with their immobile, and hence NMR invisible (for the type of experiment performed), protons which lead to sufficient contrast for the projection pursuit to have selected the image with these parameters. Fig 8(b) is essentially the same as one of the last of the original images in Fig 1, with $T_E = 100, T_R = 1000$, except for the different intensity scaling. Fig 8(c) shows marked contrast in two of the lobes, possibly due to damaged regions where cells have ruptured leading to longer T_2 values and hence higher intensity in such a T_2 -weighted image. The introduction of some T_1 weighting by reducing T_R to 745 has enhanced the contrast still further.

The reduction of the seven images in Fig 1 to three has allowed the construction of colour images such as Fig 7 which now display all the information in a single, easily-interpretable image. The possibility is thus created for the ready comparison of images derived from specimens treated in different ways, or from time courses. With the advent of cheaper colour reproduction, to the extent that the daily newspapers contain many coloured photographs, the time has surely come for the more ready publication of colour pictures in the scientific literature. It would then be essential to have a convention established which would allow such a single image to display

more than one variable in a readily assimilable form and reduce the total number of images required to convey the same information. We have chosen red and green for our colour image for the reasons given in §3.1 and believe that they give good perceived contrast severally and together as discussed.

In conclusion, we have advanced the use of statistical methods in analysing NMR images, particularly in plant microscopy. Empirical and mechanistic models of multivariate pixel values have been compared, making use of a novel reparametrisation of the mechanistic parameters to improve numerical stability. Also, a new approach has been presented to integrate the information using colour image displays, and projection pursuit has been used to identify optimal instrumental settings in synthetic images. The intention is not to usurp the experience of the spectroscopist, but rather to provide an objective assurance that the best possible combination of instrumental parameters has been selected for optimum image contrast. The creation of synthetic images can be augmented by further real time data acquisition as appropriate. The ability to depict all the information in a single, coloured image is a major step forward in rationalising the large amount of information in NMR images.

Acknowledgements

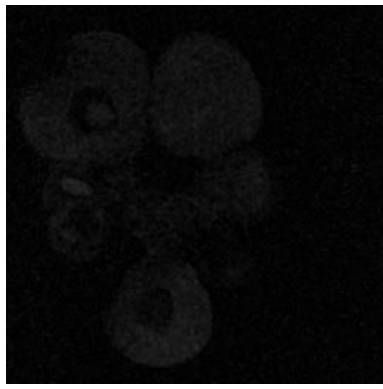
The work was supported by funds from the Scottish Executive Rural Affairs Department.

References

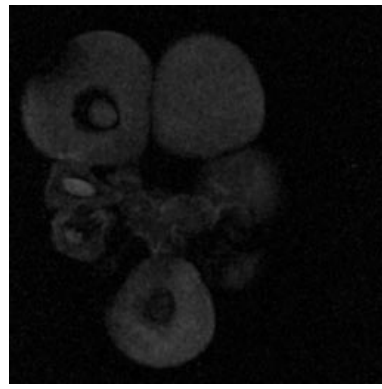
- Antalek, B., Hornak, J. P., and Windig, W. (1998). Multivariate image analysis of magnetic resonance images with the direct exponential curve resolution algorithm (DECRA). Part 2: application to human brain images. *Journal of Magnetic Resonance*, 132:307–315.
- Backfrieder, W., Baumgartner, R., Samal, M., Moser, E., and Bergmann, H. (1996). Quantification of intensity variations in functional MR-images using rotated principal components. *Physics in Medicine and Biology*, 41:1425–1438.
- Bullmore, E., Brammer, M., Williams, S. C. R., Rabeshesketh, S., Janot, N., David, A., Mellers, J., Howard, R., and Sham, P. (1996). Statistical methods of estimation and inference for functional MR image-analysis. *Magnetic Resonance in Medicine*, 35:261–277.
- Callaghan, P. T. (1991). *Principles of Nuclear Magnetic Resonance Microscopy*. Oxford University Press, Oxford.
- Cook, D., Buja, A., and Cabrera, J. (1993). Projection pursuit indexes based on orthonormal function expansions. *Journal of Computational and Graphical Statistics*, 2:225–250.
- Dreher, W. and Börnert, P. (1988). Pulse sequence and parameter choice in NMR imaging as a problem of constrained multidimensional nonlinear optimization. *Magnetic Resonance in Medicine*, 8:16–24.

- Fox, R. A. and Henson, P. W. (1986). A general method for optimizing tissue discrimination in magnetic resonance imaging. *Medical Physics*, 13:635–643.
- Garnier, S. J., Bilbro, G. L., Gault, J. W., Snyder, W. E., and Han, Y. S. (1993). Magnetic-resonance image-analysis. In *SPIE Conference on Image Modeling*, volume 21, pages 34–44.
- Geladi, P., Bengtsson, E., Esbensen, K., and Grahn, H. (1992a). Image-analysis in chemistry. 1. Properties of images, greylevel operations, the multivariate image. *TRAC-Trends In Analytical Chemistry*, 11:41–53.
- Geladi, P., Grahn, H., Esbensen, K., and Bengtsson, E. (1992b). Image-analysis in chemistry. 2. Multivariate image-analysis. *TRAC-Trends In Analytical Chemistry*, 11:121–130.
- Glad, I. K. and Sebastiani, G. (1995). A Bayesian-approach to synthetic magnetic-resonance-imaging. *Biometrika*, 82:237–250.
- Gladden, L. F. and Alexander, P. (1996). Applications of nuclear magnetic resonance imaging in process engineering. *Measurement Science and Technology*, 7:423–435.
- Glasbey, C. A. and Horgan, G. W. (1995). *Image Analysis for the Biological Sciences*. Wiley, Chichester.
- Goodman, B. A., Williamson, B., and Chudek, J. A. (1992). Nuclear magnetic resonance (NMR) microimaging of raspberry fruit: further studies on the origin of the image. *New Phytologist*, 122:529–535.
- Goodman, B. A., Williamson, B. and Simpson, E. J., Chudek, J. A., Hunter, G., and Prior, D. A. M. (1996). High field NMR microscopic imaging of cultivated strawberry fruit. *Magnetic Resonance Imaging*, 14:187–196.
- Grahn, H., Szeverenyi, N. M., Roggenbuck, M. W., Delaglio, F., and Geladi, P. (1989). Data-analysis of multivariate magnetic-resonance images. 1. A principal component analysis approach. *Chemometrics and Intelligent Laboratory Systems*, 5:311–322.
- Grahn, H. F. and Saaf, J. (1992). Multivariate image regression and analysis – useful techniques for the evaluation of clinical magnetic-resonance images. *Chemometrics and Intelligent Laboratory Systems*, 14:391–396.
- Jones, M. C. and Sibson, R. (1987). What is projection pursuit? (with discussion). *Journal of the Royal Statistical Society, Series A*, 150:1–36.
- Krzanowski, W. J. (1988). *Principles of Multivariate Analysis : A User’s Perspective*. Clarendon, Oxford.
- Lange, N. and Zeger, S. L. (1997). Nonlinear Fourier time series analysis for human brain mapping by functional magnetic resonance imaging (with discussion). *Applied Statistics*, 46:1–29.
- Lange, R. C., Duberg, A. C., and McCarthy, S. M. (1991). An evaluation of MRI contrast in the uterus using synthetic imaging. *Magnetic Resonance in Medicine*, 17:279–284.

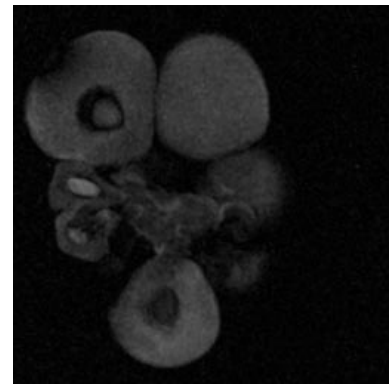
- Majumdar, S., Sostman, H. D., and MacFall, J. R. (1989). Contrast and accuracy of relaxation-time measurements in acquired and synthesized multislice magnetic-resonance images. *Investigative Radiology*, 24:119–127.
- Merickel, M. B., Berr, S., Spetz, K., Jackson, T. R., Snell, J., Gillies, P., Shimshick, E., Hainer, J., Brookeman, J. R., and Ayers, C. R. (1993). Noninvasive quantitative-evaluation of atherosclerosis using MRI and image-analysis. *Arteriosclerosis and Thrombosis*, 13:1180–1186.
- Merickel, M. B., Carman, C. S., Brookman, J. R., and Ayers, C. R. (1991). Image-analysis and quantification of atherosclerosis using MRI. *Computerized Medical Imaging and Graphics*, 15:207–216.
- Numerical Algorithms Group (1993). *Library Manual Mark 16*. NAG Central Office, 256 Banbury Road, Oxford OX2 7DE, U.K.
- Pedersen, F., Bengtsson, E., and Nordin, B. (1995). An extended strategy for exploratory multivariate image analysis including noise considerations. *Journal of Chemometrics*, 9:389–409.
- Rogowska, J., Preston, K., Hunter, G. J., Hamberg, L. M., Kwong, K. K., Salonen, O., and Wolf, G. L. (1995). Applications of similarity mapping in dynamic MRI. *IEEE Transactions on Medical Imaging*, 14:480–486.
- Ross, G. J. S. (1990). *Nonlinear Estimation*. Springer-Verlag, New York.
- Sebastiani, G. and Barone, P. (1991). Mathematical principles of basic magnetic resonance imaging in medicine. *Signal Processing*, 25:227–250.
- Sinha, S., Sinha, U., Kangarloo, H., and Huang, H. K. (1992). Magnetic-resonance image synthesis from analytic solutions of spin-echo and radio frequency-spoiled gradient-echo images. *Investigative Radiology*, 27:856–864.
- Soltanian-Zadeh, H., Windham, J. P., and Peck, D. J. (1996). Optimal linear transformation for MRI feature-extraction. *IEEE Transactions on Medical Imaging*, 15:749–767.
- Windig, W., Hornak, J. P., and Antalek, B. (1998). Multivariate image analysis of magnetic resonance images with the direct exponential curve resolution algorithm (DECRA). Part 1: algorithm and model study. *Journal of Magnetic Resonance*, 132:298–306.
- Zhu, X. P., Hutchinson, C. E., Hawnaur, J. M., Cootes, T. F., Taylor, C. J., and Isherwood, I. (1994). Magnetic-resonance image synthesis using a flexible model. *British Journal of Radiology*, 67:976–982.
- Zion, B., Chen, P. T., and McCarthy, M. J. (1995). Detection of bruises in magnetic-resonance images of apples. *Computers and Electronics in Agriculture*, 13:289–299.



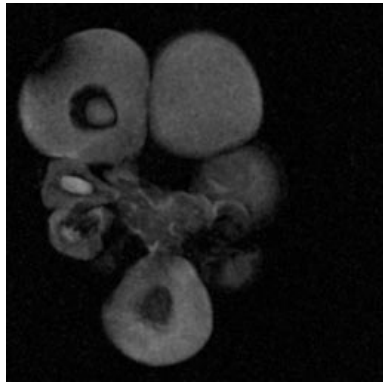
$T_E = 10, T_R = 50$



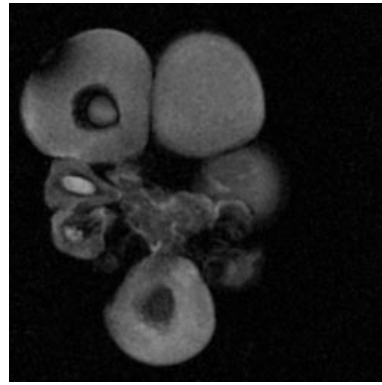
$T_E = 10, T_R = 100$



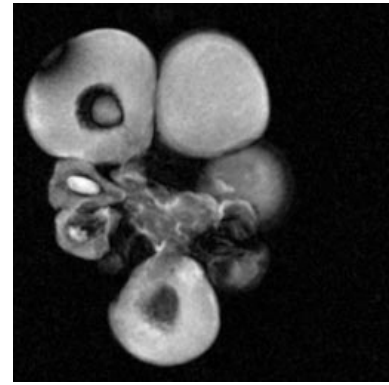
$T_E = 10, T_R = 150$



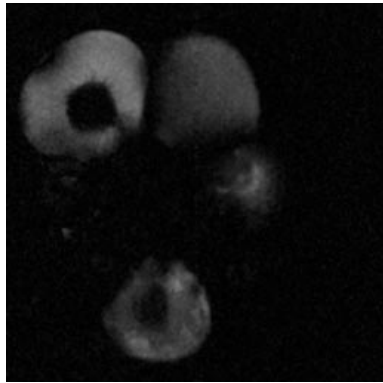
$T_E = 10, T_R = 200$



$T_E = 10, T_R = 250$



$T_E = 10, T_R = 500$



$T_E = 100, T_R = 1000$

Figure 1: *NMR microscopy cross-sections of a blackberry, for seven settings of T_E and T_R . Settings of other instrumental parameters were as follows – slice thickness: $500\mu\text{m}$; FOV: 15mm ; number of acquisitions: 2; hard 180° pulse: $32\mu\text{s}$; slice selective pulse: 2ms 3-lobed sinc pulse. (Pixel values have been standardised to a common scale from 0 to 255, with 0 shown as black and 255 as white.)*

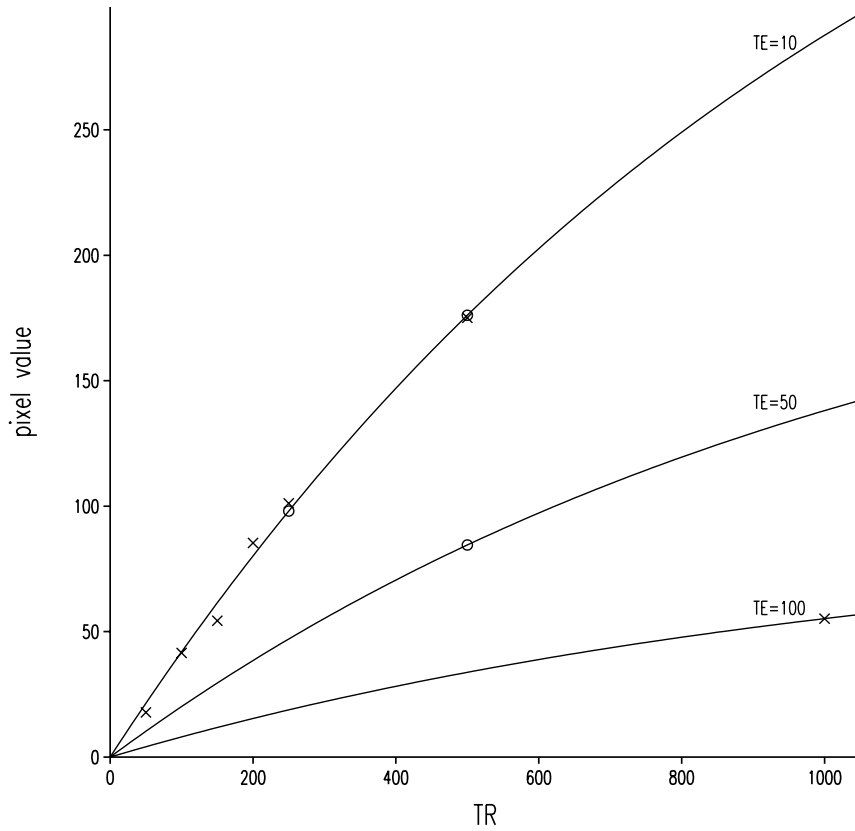
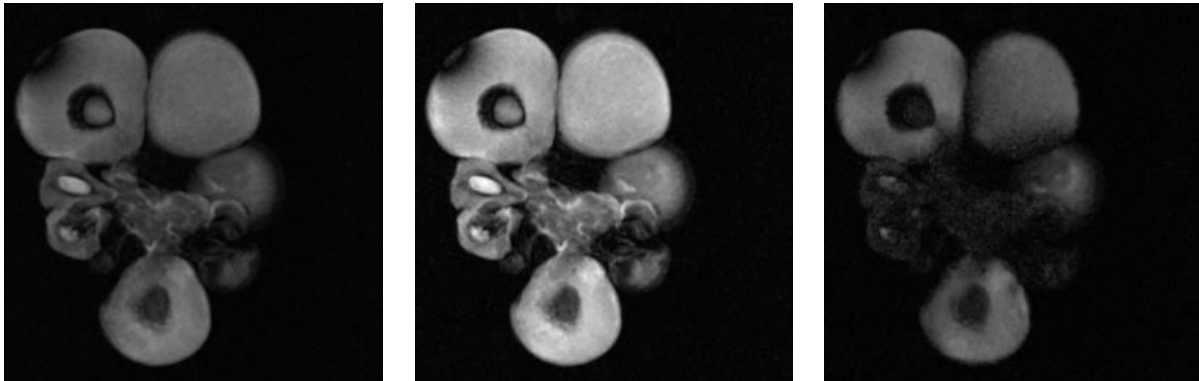


Figure 2: *Illustration of fit of mechanistic model to data for a single pixel: \times denotes the data, \circ shows the three parameters used in fitting the model, — denotes the predicted signal for three values of T_E .*



γ_1 : $T_E = 10$, $T_R = 250$

γ_2 : $T_E = 10$, $T_R = 500$

γ_3 : $T_E = 50$, $T_R = 500$

Figure 3: *Predicted images for fitted mechanistic model. (Pixel values range from 0 to 255: they are displayed on a common scale, with 0 shown as black and 255 as white.)*

	image number (j)						
	1	2	3	4	5	6	7
	means (μ_j)						
	8.8	15.1	21.2	27.5	32.5	55.0	17.0
k	variances-covariances (V_{jk}), % correlations below diagonal						
1	43	84	130	178	216	382	104
2	86.0	222	330	454	550	978	267
3	86.8	96.8	525	706	857	1527	415
4	86.8	97.2	98.4	981	1177	2101	572
5	86.6	97.2	98.6	99.1	1440	2554	699
6	86.1	96.9	98.4	99.0	99.4	4589	1272
7	63.9	72.1	73.0	73.6	74.2	75.6	616
	% coefficients of principal components (β_{jk})						
1	6.3	16.1	25.1	34.6	42.0	75.2	21.4
2	-2.3	-5.2	-8.5	-10.9	-11.7	-12.1	97.4
3	26.4	37.8	44.0	41.4	24.7	-59.7	6.6
	% coefficients of non-centred principal components (β'_{jk})						
1	8.5	17.7	26.2	35.1	42.2	73.8	21.7
2	-1.9	-5.0	-8.3	-10.9	-11.7	-12.5	97.4
3	53.2	45.1	38.8	27.0	12.8	-52.2	4.5

Table 1: *Summary statistics and principal components.*

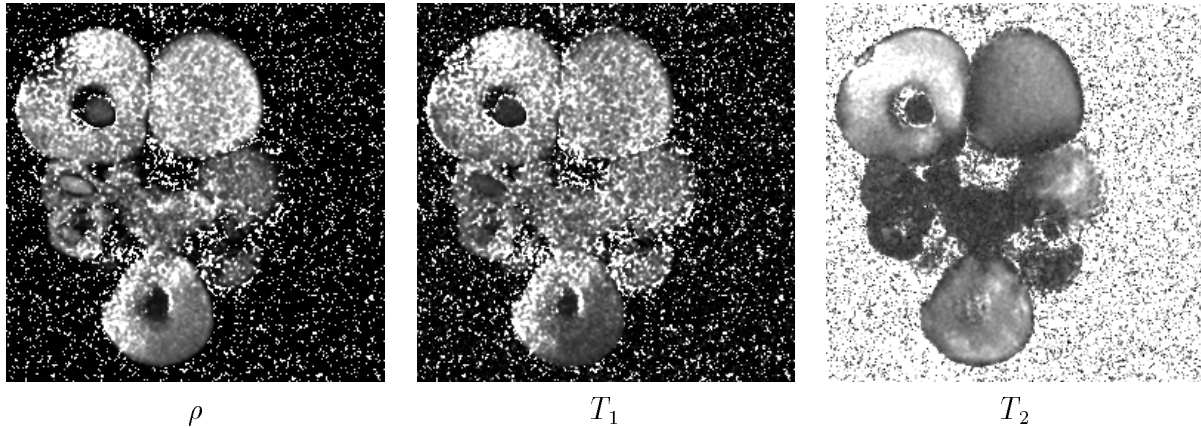


Figure 4: *Estimated parameter values for fitted mechanistic model. (Values of zero are displayed as black and those above a limit are displayed as white: the limit is 1000 for ρ , 2000 for T_1 and 100 for T_2 .)*

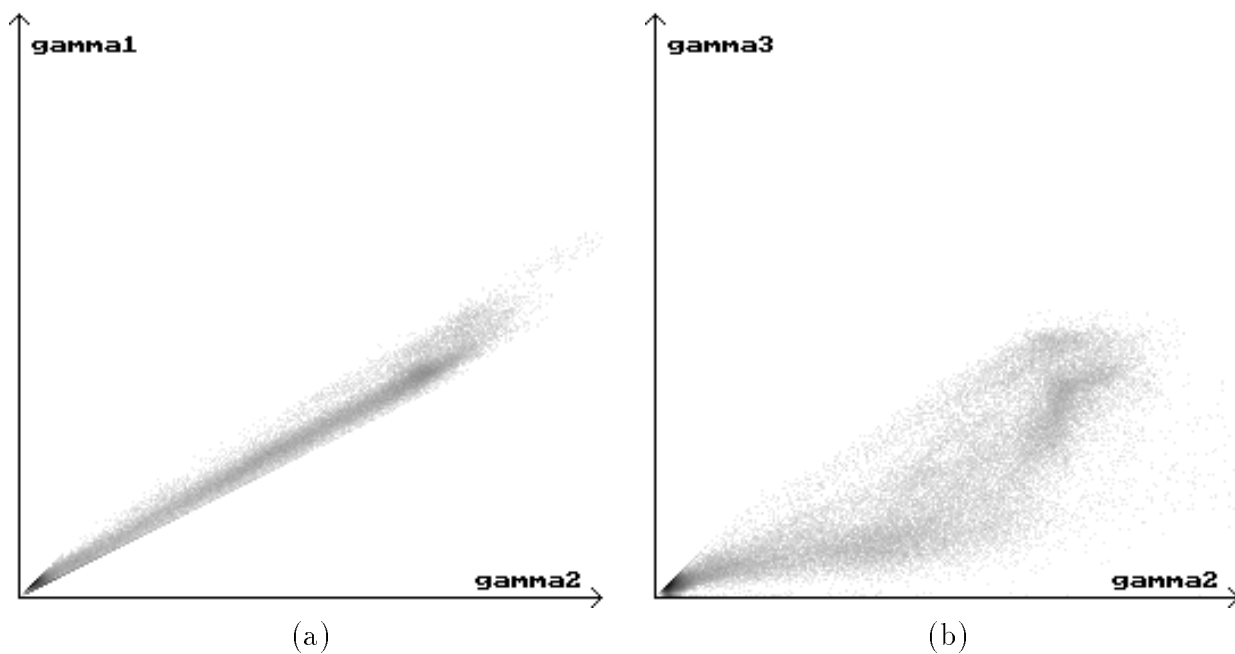


Figure 5: *Plots of pixel values in pairs of images: (a), γ_1 v. γ_2 , (b), γ_3 v. γ_2 . (The darkness of the display indicates the density of points.)*

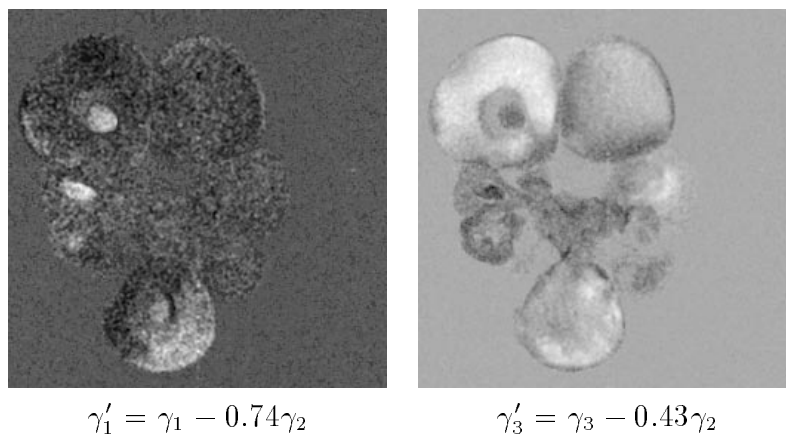


Figure 6: *Differenced images. (Negative pixel values are displayed as darker greys and positive values as lighter greys. Different scales have been used in the two images.)*

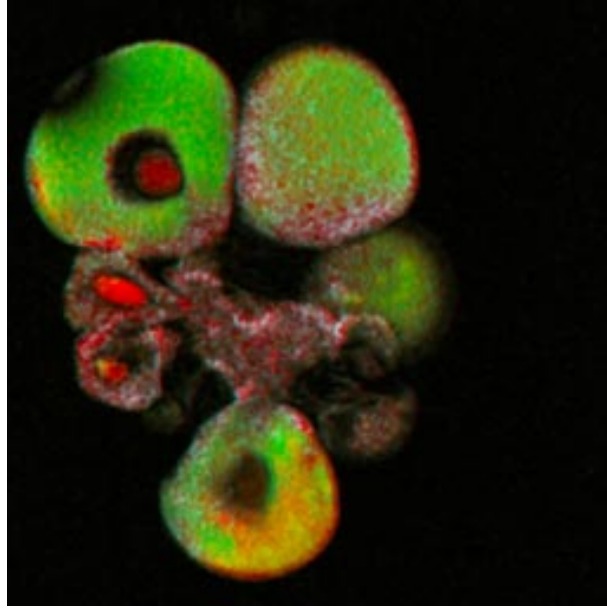
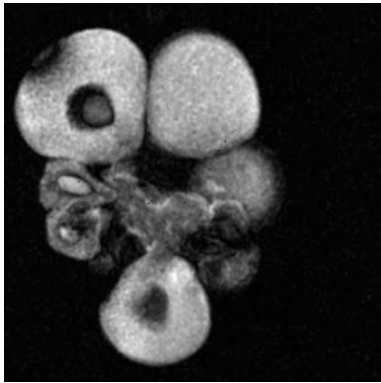
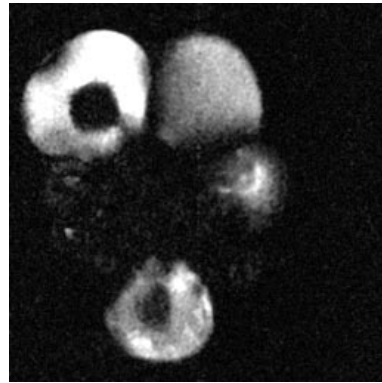


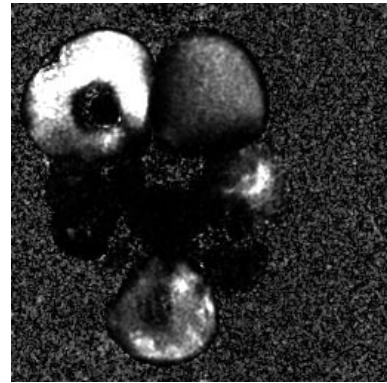
Figure 7: *Pseudo-coloured composite image (see text).*



(a): $T_E = 17$, $T_R = 1000$



(b): $T_E = 94$, $T_R = 1000$



(c): $T_E = 200$, $T_R = 745$

Figure 8: *Synthetic NMR images selected by projection pursuit to minimise entropy. (Each image has been separately scaled so that the smallest pixel value is displayed as black and the largest as white.)*